Eur. Phys. J. D (2015) 69: 165
DOI: 10.1140/epjd/e2015-60123-7

THE EUROPEAN PHYSICAL JOURNAL D

Regular Article

# Simulation of the secondary electrons energy deposition produced by proton beams in PMMA: influence of the target electronic excitation description*

Maurizio Dapor[1], Isabel Abril[2,a], Pablo de Vera[3], and Rafael Garcia-Molina[4]

[1] European Centre for Theoretical Studies in Nuclear Physics and Related Areas (ECT*-FBK) and Trento Institute for Fundamental Physics and Applications (TIFPA-INFN), via Sommarive 18, 38123 Trento, Italy
[2] Departament de Física Aplicada, Universitat d'Alacant, 03080 Alacant, Spain
[3] Department of Physical Sciences, The Open University, Walton Hall, MK7 6AA Milton Keynes, UK
[4] Departamento de Física - Centro de Investigación en Óptica y Nanofísica, Regional Campus of International Excellence "Campus Mare Nostrum", Universidad de Murcia, 30100 Murcia, Spain

Received 24 February 2015 / Received in final form 14 May 2015
Published online 25 June 2015 – 

**Abstract.** We have studied the radial dependence of the energy deposition of the secondary electron generated by swift proton beams incident with energies $T = 50$ keV–5 MeV on poly(methylmethacrylate) (PMMA). Two different approaches have been used to model the electronic excitation spectrum of PMMA through its energy loss function (ELF), namely the extended-Drude ELF and the Mermin ELF. The singly differential cross section and the total cross section for ionization, as well as the average energy of the generated secondary electrons, show sizeable differences at $T \leqslant 0.1$ MeV when evaluated with these two ELF models. In order to know the radial distribution around the proton track of the energy deposited by the cascade of secondary electrons, a simulation has been performed that follows the motion of the electrons through the target taking into account both the inelastic interactions (via electronic ionizations and excitations as well as electron-phonon and electron trapping by polaron creation) and the elastic interactions. The radial distribution of the energy deposited by the secondary electrons around the proton track shows notable differences between the simulations performed with the extended-Drude ELF or the Mermin ELF, being the former more spread out (and, therefore, less peaked) than the latter. The highest intensity and sharpness of the deposited energy distributions takes place for proton beams incident with $T \sim 0.1$–1 MeV. We have also studied the influence in the radial distribution of deposited energy of using a full energy distribution of secondary electrons generated by proton impact or using a single value (namely, the average value of the distribution); our results show that differences between both simulations become important for proton energies larger than ∼0.1 MeV. The results presented in this work have potential applications in materials science, as well as hadron therapy (due to the use of PMMA as a tissue phantom) in order to properly consider the generation of electrons by proton beams and their subsequent transport and energy deposition through the target in nanometric scales.

## 1 Introduction

Energetic ion beams are an excellent tool for many purposes. Already well-known as a useful instrument in microelectronics and nanofabrication techniques, one of their most promising use is the treatment of deep-seated tumors, because ion beams offer enhanced selectivity and relative biological effectiveness as compared to conventional photon and electron radiotherapy [1,2]. The physical properties of swift protons produce a depth-dose distribution characterized by a nearly flat and small dose at the entrance in the tissue and during the major part of the projectile path in the target, with a sharp maximum close to the end of the range, known as the Bragg peak, and with a strong fall-off at the distal edge. Another advantage of energetic ion beams is their well-defined range, as well as their small lateral spread, which allow modern scanning beam systems to impart the dose with millimeter precision [3]. The inherent ability to precisely control the proton dose deposition in the patient makes hadron therapy very attractive, permitting maximum energy delivery to tumor cells while minimizing the dose imparted to the normal tissue regions adjacent to the tumor [4].

* Contribution to the Topical Issue "COST Action Nano-IBCT: Nano-scale Processes Behind Ion-Beam Cancer Therapy", edited by Andrey Solov'yov, Nigel Mason, Gustavo García, Eugene Surdutovich.

[a] e-mail: ias@ua.es

During the propagation of fast ions through organic targets, the main channels of energy loss are the electronic excitation and ionization processes, which induce the generation of a large number of secondary electrons, followed by their subsequent propagation in a nanometer scale [5]. Low energy electrons (LEEs, with typical energies below 100 eV) are the most abundant and carry most of the energy lost by the initial fast particles, being one of the main responsible for radiation damage, due to dissociative electron attachment [6,7]. Therefore, the propagation and interaction of LEEs with organic targets is an important part of the assessment of the total radiation damage induced by the primary radiation. Indeed, the propagation of LEEs around the ion tracks gives place to very sharp radial dose distributions at the nanometer scale, which are one of the main inputs for radiation damage models that allow the calculation of the effect of radiation in the target [8], being it of biological (cell killing) or non-biological (detector response, material damage) nature.

In this work, we study theoretically and by simulation the generation of secondary electrons in the organic material PMMA by the impact of energetic protons, as well as their propagation, generation of new electron cascades and the final energy deposition in the target by all the electrons. The combined effects of all these processes give place to nanometric radial energy deposition distributions around the proton track. The energy range of the impinging protons is taken from 50 keV to 5 MeV, which corresponds to representative energies around the Bragg peak [9,10]. The PMMA target is chosen in this study because it is a material of interest, both in hadron therapy as well as in nanofabrication. This material is considered as a water-equivalent material, having density and electronic properties quite similar to those of liquid water [11], hence being frequently used as a solid water or tissue phantom in order to facilitate dosimetry measurements [12]. It is employed as well in microelectronics, since it is a common resist in nanolitographic techniques [13].

This paper is organized as follows. First, in Section 2, we describe a semiempirical model to calculate the energy distribution of the ejected secondary electrons due to the impact of energetic protons in PMMA. This model [14] is based on the dielectric formalism and assumes that the weak bound electrons of the target can be characterized by a mean binding energy, which allows the calculation of the initial energy distribution of the ejected secondary electrons by the proton impact. The influence of the target electronic excitation spectrum description by Drude or Mermin energy loss functions will also be evaluated. Section 3 is devoted to the propagation of the initially generated electrons through the medium, which is done by means of a Monte Carlo simulation, where elastic and inelastic collisions are properly taken into account. The former leads to changes in electron direction, whereas the later accounts for energy transferred to the medium (either by ionization or excitation), which creates additional electrons that also are followed by our simulation code. Finally, in Section 4, the results for the nanoscopic radial energy deposition distribution around the ion track are presented. This quantity gives an immediate idea of the range of distances from the track where the energy is deposited and provides quantitative inputs for detailed damage estimations. The conclusions and summary of the paper are outlined in Section 5.

## 2 Initial energy distributions of secondary electrons generated by proton impact

The dominant slowing down mechanism for swift protons traveling through a condensed target is the electronic energy loss, including excitations and ionization of the target electrons. For a condensed target we use the dielectric formalism to calculate its electronic response to the passage of charged particles [15,16]. For a proton with kinetic energy $T$, moving through a condensed target characterized by its dielectric function $\varepsilon(k,\omega)$, with $\hbar k$ and $\hbar\omega$ being the momentum and energy transferred in an inelastic collision, the generation of secondary electrons by the incoming proton can be obtained assuming that the weakly-bound (outer-shell) electrons of the target are characterized by a mean binding energy $\bar{B}$ [14]. If $\hbar\omega > \bar{B}$, a secondary electron will be ejected with a kinetic energy $W_0 = \hbar\omega - \bar{B}$. For inner-shell electrons, characterized by their ionization energy $B_{\mathrm{ioniz},j}$, the secondary electrons will be emitted with a kinetic energy $W_0 = \hbar\omega - B_{\mathrm{ioniz},j}$. The energy spectrum of the electrons is given by the ionization singly differential cross section (SDCS) $d\sigma_{\mathrm{ioniz}}(T,W_0)/dW_0$, which is [14,17]

$$\frac{d\sigma_{\mathrm{ioniz}}(T,W_0)}{dW_0} = \frac{e^2}{\pi\hbar^2}\frac{M}{T}\frac{1}{N}\int_{k_1}^{k_2}\frac{dk}{k} \times \left\{ \mathrm{Im}\left[\frac{-1}{\varepsilon\left(k,\left(W_0+\bar{B}\right)/\hbar\right)}\right]_{\mathrm{outer}} + \sum_j \mathrm{Im}\left[\frac{-1}{\varepsilon\left(k,\left(W_0+B_{\mathrm{ioniz},j}\right)/\hbar\right)}\right]_{\mathrm{inner}} \right\} \quad (1)$$

where $e$ is the elementary charge, $M$ is the proton mass and $N$ is the molecular density of the target. The integration limits $k_{2,1} = \sqrt{2M}(\sqrt{T} \pm \sqrt{T-\hbar\omega})/\hbar$ of the $k$-integral result from momentum conservation laws. According to equation (1), the energy loss function (ELF) of the target, $\mathrm{Im}[-1/\varepsilon(k,\omega)]$, completely determines the initial energy distribution of the generated electrons due to inelastic events. The first (second) summand in the integrand refers to the outer (inner) shell electrons contribution to the ELF. Therefore, in order to proceed with the integrations appearing in equation (1) it is necessary to know the ELF over all the $k$-$\omega$ plane, i.e., the Bethe surface of the material.

In the description of the electronic excitation properties of PMMA, with a chemical formula $(C_5H_8O_2)_n$, we consider as inner-shell electrons the K-shell of C and O, with ionization energies $B_{\mathrm{ioniz},j}$ of 284.2 and 543.1 eV, respectively. The contribution of these electrons to the ELF

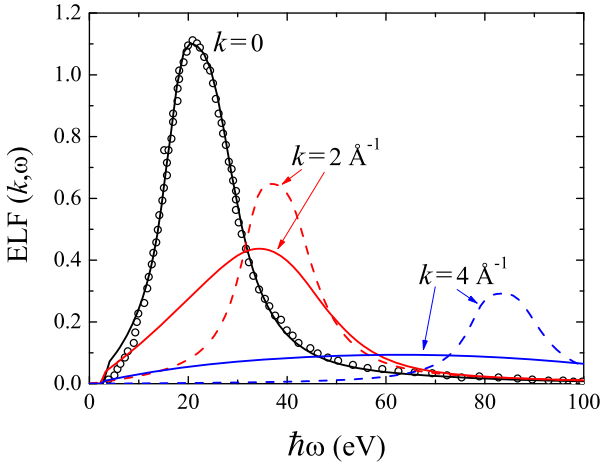


**Fig. 1.** Energy loss function (ELF) of PMMA as a function of the transferred energy $\hbar\omega$, for several values of the momentum transfer $\hbar k$. Symbols correspond to the experimental optical data from [19]. Solid (dashed) lines correspond to the Mermin (extended-Drude) descriptions of the ELF. Notice that at the optical limit ($k = 0$) both ELF models are identical.

will be described by their hydrogenic generalized oscillator strengths (GOS), which are suitable for atomic cores, where bonding effects can be ignored [18]. The outer-shell electron excitation spectrum is accounted for by optical data models with $\bar{B} = 20$ eV [17], where experimental data for the ELF at the optical limit (i.e., at $k = 0$) are used, while its extrapolation to finite momentum transfers ($k \neq 0$) is provided by suitable extension algorithms. It is possible to obtain experimental optical information for PMMA [19] from electron energy-loss spectroscopy measurements over the valence electron excitation range ($\hbar\omega \leqslant 100$ eV) which exhibits a well defined peak at about the nominal plasmon energy (∼20 eV), as it is usual in many organic and biological materials. The experimental optical ELF is analytically parameterized by a weighted sum of Drude-type ELF functions [20]:

$$\mathrm{Im}\left[\frac{-1}{\varepsilon(k=0,\omega)}\right]_{\mathrm{exp}} = \sum_i \frac{A_i}{\omega_i^2}\mathrm{Im}\left[\frac{-1}{\varepsilon_{\mathrm{D}}(k=0,\omega;\omega_i,\gamma_i)}\right] = \sum_i A_i \frac{\omega\,\gamma_i}{(\omega_i^2-\omega^2)^2+(\omega\,\gamma_i)^2} \quad (2)$$

where $\varepsilon_{\mathrm{D}}$ is the Drude dielectric function and the parameters $\omega_i$, $\gamma_i$ and $A_i$ that characterize, respectively, the position, width and intensity of each peak in the experimental energy-loss spectrum of PMMA are given in reference [21]. The use of the experimental optical ELF accounts for the phase and aggregation effects of the target. Besides resembling the experimental optical ELF, the built ELF fulfills the $f$-sum rule and the KK sum rule [22,23]. Figure 1 shows by symbols the experimental ELF of PMMA at the optical limit [19], together with the parameterization (solid line) from [21].

To calculate the energy spectrum of the generated secondary electrons by using equation (1), it is necessary to know or to model the target ELF over the complete energy- and momentum- transfer range, i.e. the Bethe surface. We consider here two different procedures to extend the ELF to $k \neq 0$ values:

(i) the extended-Drude model [24] where the $k$-dependence of the energy coefficient $\omega_i$ follows a quadratic dispersion relation that in the random phase approximation (RPA) is:

$$\omega_i(k) = \omega_i(k=0)+\alpha_{\mathrm{RPA}}\frac{\hbar k^2}{2m} \simeq \omega_i(k=0)+\frac{\hbar k^2}{2m}, \quad (3)$$

where $m$ is the electron mass, and $\alpha_{\mathrm{RPA}} = 6\omega_{\mathrm{F}}/(5\omega_{\mathrm{pl}}) \simeq 1$ for PMMA, since the free-electron Fermi and plasmon energies are $\hbar\omega_{\mathrm{F}} = 19.3$ eV and $\hbar\omega_{\mathrm{pl}} = 23$ eV, respectively. On the other hand, no dispersion was assumed for the damping coefficient, i.e. $\gamma_i(k) = \gamma(k=0)$.

(ii) the MELF (Mermin Energy Loss Function) method [25,26] where the outer electron excitations are automatically dispersed following the properties of the Mermin ELF:

$$\mathrm{Im}\left[\frac{-1}{\varepsilon(k,\omega)}\right]_{\mathrm{MELF}} = \sum_i \frac{A_i}{\omega_i^2}\mathrm{Im}\left[\frac{-1}{\varepsilon_{\mathrm{M}}(k,\omega;\omega_i,\gamma_i)}\right], \quad (4)$$

where $\varepsilon_{\mathrm{M}}$ is the Mermin dielectric function [27]. In this case it is not necessary to presume a dispersion relation for the $k$-dependence, because the momentum dispersion is given automatically through the analytical properties of the Mermin dielectric function. It is worth to notice that the values of the parameters $\omega_i$, $\gamma_i$ and $A_i$ are the same for both, the Drude and the Mermin-ELF at the optical limit.

Both ELF models (extended-Drude and Mermin ELF) are identical at the optical limit, the inner-shell electron excitations are included by the GOS in both cases, and the only difference is their extension for outer electrons to arbitrary values of the momentum transfer. In Figure 1 we show the ELF at two values of the momentum transfer ($k = 2$ and $4$ Å$^{-1}$), calculated by the extended-Drude model (dashed lines) and by the MELF model (solid lines). Whereas in the former the evolution of the ELF preserves its initial shape with a slight reduction, the latter gives a pronounced broadening and a reduction of the intensity of the ELF. This result is in good agreement with the fact that single-particle excitations prevail over collective excitation as the momentum transfer increases due to the plasmon damping. The dispersion of the damping coefficient, only considered (implicitly) in the MELF model, provides the expected momentum broadening of the Bethe ridge; the results from the MELF model agree better than those from the extended-Drude model with the few experimental data at $k \neq 0$ measured for graphite [28,29], aluminum [30,31] or liquid water [20,32,33].

We present in Figure 2 the calculated secondary electron energy distributions generated in PMMA due to the impact of protons, equation (1), at several energies $T$ of the incident proton beam. The range of proton energies is chosen from 50 keV to 5 MeV, which are typical projectile

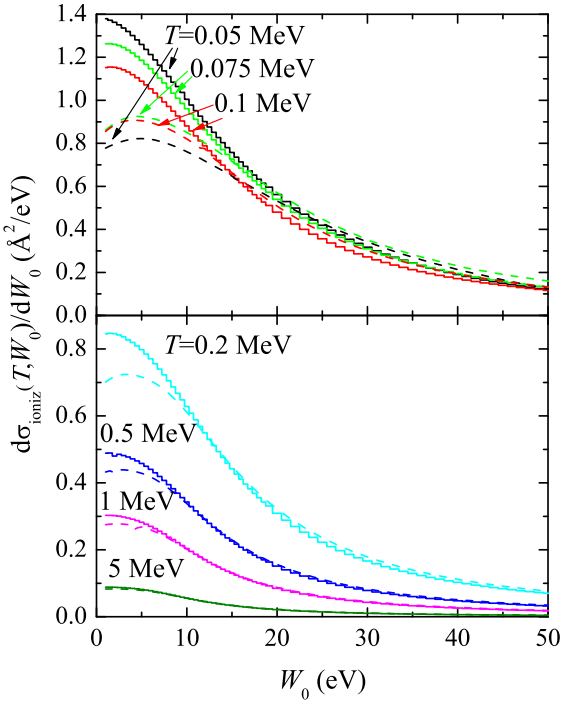


**Fig. 2.** Energy distribution of secondary electrons (ionization-SDCS: $d\sigma_{\rm ioniz}/dW_0$) produced by energetic protons in PMMA, as a function of the kinetic energy $W_0$ of the emitted electrons. $d\sigma_{\rm ioniz}/dW_0$ is obtained at several initial proton energies $T$. Calculations done with the MELF-GOS model are depicted by solid lines, whereas results from the extended-Drude-GOS model are shown by dotted lines.

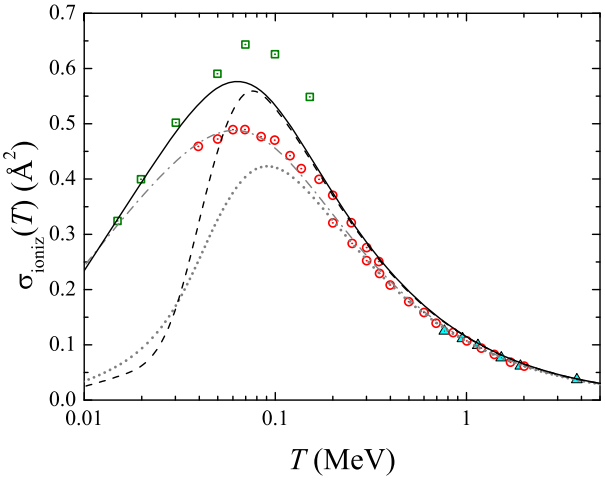


**Fig. 3.** Total ionization cross section (TICS) $\sigma_{\rm ioniz}$, for protons in PMMA, as a function of the incident energy $T$ calculated by the MELF-GOS (solid line) and the extended-Drude-GOS (dashed line) models. $\sigma_{\rm ioniz}$ for protons in liquid water is calculated by the MELF-GOS (gray dash-dotted line) and the extended-Drude-GOS (gray dotted line) models. Experimental data for water vapor are represented by triangles [34], circles [35] and squares [36].

energies around the Bragg peak [9,10]. Without entering into the differences between the predictions of both ELF models, first, we can observe that most of the secondary electrons generated are in the low-energy range. Second, the number of generated electrons increases when the proton energy decreases, meaning that at the Bragg peak there is a strong increment in the ionization of the target, being larger than in the plateau of the Bragg curve, where the proton energy is larger. Third, the influence of the target ELF modeling in the ionization-SDCS is larger for lower proton energies. A detailed comparison of the energy spectrum of the generated secondary electrons derived from the MELF-GOS model (solid lines) and from the extended-Drude-GOS model (dashed lines) shows that $d\sigma_{\rm ioniz}/dW_0$ is always larger for the MELF-GOS description than for the Drude description of the ELF, and these differences increase when the energy of the incoming proton decreases. So, at proton energies larger than 5 MeV, $d\sigma_{\rm ioniz}/dW_0$ is almost independent of the ELF description. On the other hand, the energy distribution of the generated secondary electrons is peaked at very low energies, so for the MELF-GOS model the probability to generate secondary electrons with kinetic energy of $W_0 = 50$ eV represent around 10% of the electrons generated at $W_0 = 10$ eV, whereas for the electrons with $W_0 = 100$ eV represents only 2–4%, this behavior being the same for all the proton energies analyzed.

The total ionization cross section (TICS), $\sigma_{\rm ioniz}(T)$, is given by:

$$\sigma_{\rm ioniz}(T) = \int_0^{T_{\rm max}} \frac{d\sigma_{\rm ioniz}(T, W_0)}{dW_0}\, dW_0, \qquad (5)$$

where $T_{\rm max} = 4mT/M$ is the maximum energy transferred in the collision. The calculated $\sigma_{\rm ioniz}$ for protons in PMMA is shown in Figure 3 for both of the discussed ELF descriptions: MELF-GOS (solid line) and extended-Drude-GOS (dashed line). We find that at high proton energies ($\geqslant$200 keV) the TICS is independent of the ELF description. However, as the proton energy decreases significant differences appear in the values of $\sigma_{\rm ioniz}$ depending on the ELF description. For a proton energy $T = 50$ keV, $\sigma_{\rm ioniz} = 0.56$ Å$^2$ when the MELF-GOS model is used and $\sigma_{\rm ioniz} = 0.46$ Å$^2$ for the extended-Drude-GOS method; whereas for $T = 30$ keV, $\sigma_{\rm ioniz}$ are, respectively, 0.48 Å$^2$ and 0.16 Å$^2$ when the MELF-GOS or the extended-Drude-GOS description for the ELF is applied.

For comparative purposes, the $\sigma_{\rm ioniz}$ for protons in liquid water is also depicted in Figure 3, showing values that are lower than those corresponding to PMMA in all the energy range. Analogously to the PMMA results, for liquid water there are important differences in the $\sigma_{\rm ioniz}$ values depending on the ELF description (gray dash-dotted line for the MELF-GOS and gray dotted line for the extended-Drude-GOS) as it is depicted in Figure 3 [14,17]. However, in this case there are experimental data of $\sigma_{\rm ioniz}$ for proton impact in water vapor to compare with [34–36], which are shown by symbols in Figure 3. For liquid water the calculated $\sigma_{\rm ioniz}$ using the MELF-GOS description of the ELF agrees very well with the experimental data from [34,35]

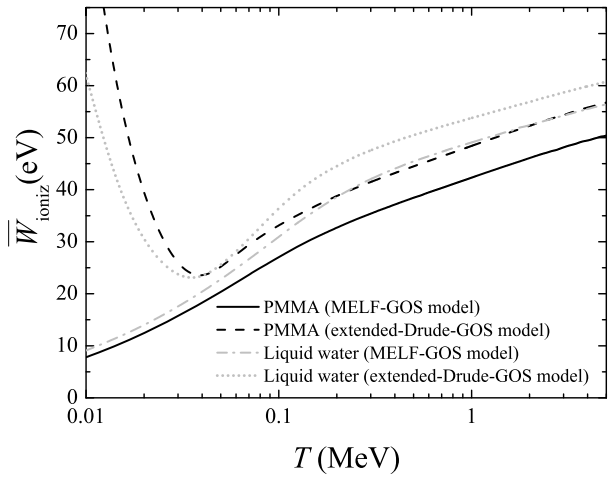


**Fig. 4.** Average energy $\overline{W}_{\text{ioniz}}$ of the secondary electrons generated in PMMA by the impact of energetic protons as a function of their energy $T$. Calculations by the MELF-GOS model are shown by a solid line and by the extended-Drude-GOS model by a dashed line. Results of $\overline{W}_{\text{ioniz}}$ for protons in liquid water are also reported: MELF-GOS (gray dash-dotted line) and extended-Drude-GOS (gray dotted line).

in all the proton energy range, a fact that indicates that the MELF-GOS description of the energy-loss spectrum is more realistic than the extended-Drude one.

As it can be seen in Figure 3, the ionization in PMMA due to proton impact is 15% larger than in liquid water around the maximum of $\sigma_{\text{ioniz}}$. Our conclusion is that the MELF-GOS model to describe the electronic excitation of the target is more precise than the extended-Drude model and that larger ionization probabilities are expected in PMMA in comparison with liquid water.

Other interesting quantity is the average energy of the ejected secondary electrons due to the proton impact, which is given by:

$$\overline{W}_{\text{ioniz}}(T) = \frac{1}{\sigma_{\text{ioniz}}(T)} \int_0^{T_{\max}} W_0 \frac{d\sigma_{\text{ioniz}}(T, W_0)}{dW_0}\, dW_0. \quad (6)$$

Our results for protons in PMMA and in liquid water are presented for the two descriptions of the ELF in Figure 4 as a function of the incoming proton energies.

We obtain larger results of $\overline{W}_{\text{ioniz}}$ for liquid water (≈10–15%) than for PMMA for all the proton energies analyzed, which means that the secondary electrons generated by proton impact in liquid water will have larger kinetic energies than those generated in PMMA targets. When the MELF-GOS model is used, $\overline{W}_{\text{ioniz}}$ for PMMA goes from ∼8 eV up to 50 eV when the proton energy changes from 10 keV to 5 MeV. With the extended-Drude model larger values of $\overline{W}_{\text{ioniz}}$ are obtained than with the MELF-GOS model with a strong unexpected growth at low projectile energies. Therefore, it is worth to notice that at low proton energies the extended-Drude model does not work properly.

## 3 Simulation of the electron transport and further generation

The generation of secondary electrons by the impact of swift ions is only the first step in the energy deposition mechanism that leads to the (possible) damage of the target. These electrons can propagate, also producing more electrons in their way (leading to a secondary electron avalanche), depositing their initial energy in nanometric volumes around the ion track, where the final effects of the energy lost by the ionic projectiles will take place. Such a scenario is generally simulated by means of Monte Carlo codes [37], which appropriately account for the stochastic behavior of radiation transport in condensed media, treating each interaction between the energetic particles with the medium individually, event-by-event, until the particle energy falls below a specified threshold [13]. Also, analytical techniques can be employed when some simplifying approximations can be assumed [38].

In this section we briefly describe a Monte Carlo simulation code, which will be used to study the propagation of the electron avalanche produced by the electrons generated by the proton impact. In this code, the transport through the target of all primary and secondary electrons is followed by an event-by-event procedure. Most of the secondary electrons initially generated by proton collisions, as shown in the previous section, have low energies, the average being of the order of several tens of eV, so they will travel in the medium distances of the order of nanometers around the ion track [5]. In their path through the target, energetic electrons undergo elastic and inelastic interactions with the medium, so it is necessary to know as input the cross sections for all the interaction processes. If we assume that the stochastic scattering process follows Poisson statistics, then the step length $\Delta s$ between successive interactions is given by $\Delta s = -\lambda \ln \eta_1$, with $\eta_1$ being a random number uniformly distributed in the interval [0,1], and $\lambda$ being the total electron mean free path, given by:

$$\lambda^{-1} = \lambda_{\text{elastic}}^{-1} + \lambda_{\text{inelastic}}^{-1}, \quad (7)$$

where $\lambda_{\text{elastic}}$ and $\lambda_{\text{inelastic}}$ are, respectively, the elastic and inelastic electron mean free paths.

Regarding the elastic collisions, since the masses of the electrons and the atoms with which they scatter are so different, we can consider them as perfectly elastic. Thus, the total and differential elastic scattering cross sections, the later one giving the probability of scattering in the polar angle $\theta$, can be calculated through the Mott theory [39], which is done solving the Dirac equation in a central field. The azimuthal angle is uniformly distributed in the range $[0, 2\pi]$.

On the other hand, electrons can lose energy via different inelastic processes, such as (i) electronic excitation and ionization of the target; (ii) electron-phonon interaction; and (iii) electron trapping by polaron creation (i.e., by polarizing the molecules around it, creating a "cage" that traps and stops the electron). Therefore, the inverse inelastic electron mean free path, $\lambda_{\text{inelastic}}^{-1}$, which takes into account all these inelastic scattering mechanisms, can be

written as:

$$\lambda^{-1}_{\text{inelastic}} = \lambda^{-1}_{\text{electronic}} + \lambda^{-1}_{\text{phonon}} + \lambda^{-1}_{\text{polaron}}. \quad (8)$$

For electron energies higher than ∼20–50 eV, the main mechanism of inelastic scattering and energy loss is their interaction with collective electronic excitations (plasmons) as well as individual electronic transitions. These inelastic energy loss mechanisms are described by the dielectric approach with the extended optical data model, as it was described in Section 2. So, the electronic inverse mean free path, $\lambda^{-1}_{\text{electronic}}$, of an electron with velocity $v$ and kinetic energy $W = mv^2/2$, is given by [21]:

$$\lambda^{-1}_{\text{electronic}}(W) = \frac{2e^2}{\pi v^2} \int_0^{\omega_{\max}} d\omega \times \int_{k_{e1}}^{k_{e2}} f_{\text{exchange}}(k)\,\text{Im}\left[\frac{-1}{\varepsilon(k,\omega)}\right]\frac{dk}{k}, \quad (9)$$

where the integration limits in $k$ are $k_{e2,e1} = \sqrt{2m}(\sqrt{W} \pm \sqrt{W - \hbar\omega})/\hbar$. Due to the indistinguishability between the incident (or primary) electron and the hitted target electron, the maximum energy transferred in a collision will be $\hbar\omega_{\max} = mv^2/4$, since primary electrons are usually regarded as the most energetic after the collision. The exchange effect between the incident electron and the target electrons is also taken into account by the Born-Ochkur approximation [21,40], which introduces the function

$$f_{\text{exchange}}(k) = \left[1 - \left(\frac{\hbar k}{mv}\right)^2 + \left(\frac{\hbar k}{mv}\right)^4\right]$$

in the integrand of equation (9). The Pauli uncertainty principle is considered in the calculations as well. As we explained in Section 2, we split the target ELF in outer-shell and inner-shells components. The inner-shell ELF is described by the GOS model whereas the outer-shell ELF can be described either by the extended-Drude model [24] or the Mermin-ELF model [25,26], as already discussed.

We show in Figure 5 the electronic mean free path $\lambda_{\text{electronic}}$ for electrons in PMMA as a function of their kinetic energy $W$ and for the two different descriptions of the ELF analyzed here. For energies larger than 100 eV, $\lambda_{\text{electronic}}$ is practically insensitive to the ELF description, although at lower energies there are larger discrepancies between the results obtained with the Mermin-ELF (solid line) or with the extended-Drude ELF (dashed line), being more pronounced as the electron energy decreases. These differences in $\lambda_{\text{electronic}}$ are due to the different methods used to extend the PMMA optical ELF to non-zero momentum transfers in the Mermin-ELF and in the extended-Drude ELF. Indeed, it was already demonstrated that in the case of liquid water, where there are experimental data for the ELF at non-zero momentum transfers [32,33], the results of MELF-GOS model agree very well with the experiments, whereas those of the extended-Drude-GOS ELF do not agree so well [20]. The influence of

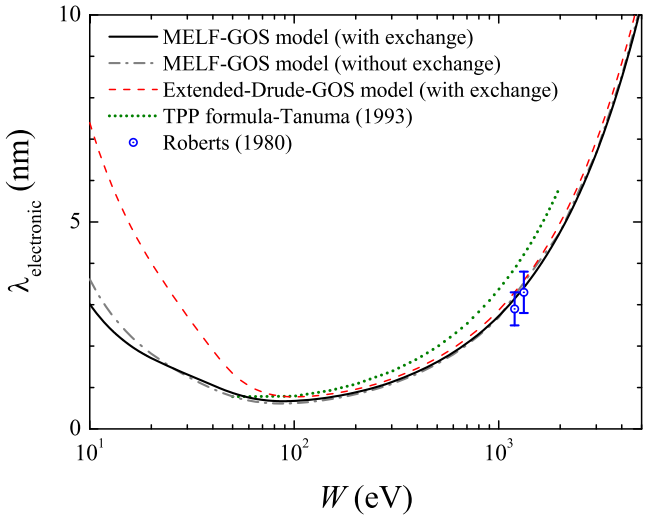


**Fig. 5.** Inelastic electronic mean free path $\lambda_{\text{electronic}}$ of electrons in PMMA as a function of their kinetic energy $W$ obtained from the MELF-GOS model (solid line) and from the extended-Drude-GOS model (dashed line). The influence of the exchange factor in $\lambda_{\text{electronic}}$ is also presented for the MELF-GOS model (gray dashed-dotted line). The experimental data from Roberts et al. [42] are also presented for comparison, as well as the prediction from the TPP formula [41] (dotted line).

the exchange factor is only visible at very low electron energies (⩽10 eV). It must be considered as an upper limit in $\lambda_{\text{electronic}}$, since the Born-Ochkur approximation is based on the single-electron excitations assumption, while our ELF description does not distinguish between single and collective excitations. The calculations obtained from the popular TPP formula [41] (dotted line) are also depicted in the figure for comparison purposes. The experimental data from [42], shown by symbols, agree well with our calculations within their uncertainty, whereas the differences are larger with the prediction from the TPP formula [41].

For electron-electron collisions, the primary electron polar scattering angle $\theta$ and the secondary electron polar ejection angle are calculated within the classical binary collision model by $\frac{\mathcal{W}}{W} = \sin^2\theta$, where $\mathcal{W}$ is the electron energy loss and $W$ is the incident electron energy. The azimuthal angle is simply obtained drawing a uniformly distributed random number in the range $[0, 2\pi]$.

For electrons with energies $W$ lower than ∼10–20 eV, the dielectric formalism is no longer able to accurately describe energy loss phenomena. In this region, electrons lose energy in many small amounts interacting with phonons, in particular with the optical modes of lattice vibrations. Therefore, the electron-phonon interaction can be described through the interaction of free conduction electrons with the longitudinal optical mode of lattice vibrations [43]. As the dispersion relation of the longitudinal phonons can be neglected in the optical branch [44], a single phonon frequency $\omega_{\text{ph}}$ can be used, and the inverse inelastic mean free path for electron (with energy $W$)-phonon interaction $\lambda^{-1}_{\text{phonon}}$ can be calculated by the

following expression [45]:

$$\lambda^{-1}_{\text{phonon}}(W) = \frac{1}{a_0}\left[\frac{n(\mathcal{T})+1}{2}\right]\left[\frac{\varepsilon(0)-\varepsilon(\infty)}{\varepsilon(0)\,\varepsilon(\infty)}\right]\frac{\hbar\omega_{\text{ph}}}{W} \times \ln\left[\frac{1+(1-\hbar\omega_{\text{ph}}/W)^{1/2}}{1-(1-\hbar\omega_{\text{ph}}/W)^{1/2}}\right], \quad (10)$$

where $n(\mathcal{T}) = (e^{\hbar\omega_{\text{ph}}/k_{\text{B}}\mathcal{T}} - 1)^{-1}$ is the occupation function for a temperature $\mathcal{T}$ of the target, $a_0$ is the Bohr radius, $k_{\text{B}}$ is the Boltzmann constant, and $\varepsilon(0)$ and $\varepsilon(\infty)$ are, respectively, the static and high frequency dielectric constant.

For the electron-phonon collisions, the scattering angle $\theta$ can be obtained, according to [45], by the expression:

$$\cos\theta = \left(\frac{W+W'}{2\sqrt{WW'}}\right)(1-G^{\eta_2}) + G^{\eta_2}, \quad (11)$$

where $G = \frac{W+W'+2\sqrt{WW'}}{W+W'-2\sqrt{WW'}}$, being $W$ and $W'$, respectively, the electron energies before and after the electron-phonon scattering, and $\eta_2$ a random number uniformly distributed in the interval $[0, 1]$. As usual, the azimuthal angle is obtained uniformly distributed in the range $[0, 2\pi]$.

A low-energy electron traversing an insulating material, such as PMMA, can polarize the medium surrounding it, creating a quasi-particle known as a "polaron", which stabilizes the electron that generates it. According to [44], the inverse inelastic mean free path for the electron (with energy $W$)-polaron interaction $\lambda^{-1}_{\text{polaron}}$, with the low-energy electron being trapped in the ionic lattice, is given by:

$$\lambda^{-1}_{\text{polaron}}(W) = C\,e^{-\Gamma W}, \quad (12)$$

where $C$ and $\Gamma$ are constants depending on the material under investigation. For PMMA we use the values $C = 1.5\ \text{nm}^{-1}$ and $\Gamma = 0.14\ \text{eV}^{-1}$ [46].

To summarize, the electrons follow stochastic trajectories, with scattering events separated by straight paths having a distribution of step lengths that follows a Poisson-type law, according to the inverse total inelastic mean free path, equation (8), which is built adding the contributions of the electronic interactions $\lambda^{-1}_{\text{electronic}}$, equation (9), the electron-phonon interaction $\lambda^{-1}_{\text{phonon}}$, equation (10), and the electron-polaron interaction $\lambda^{-1}_{\text{polaron}}$, equation (11). Once the step length is obtained, the elastic or inelastic nature of the scattering event, the polar and azimuthal angles, as well as the energy losses, are all sampled using the relevant cumulative probabilities according to the usual Monte Carlo recipes [47]. As each secondary electron produces further secondary electrons during its travel inside the target, it is therefore mandatory to follow the whole electron cascade in order to obtain quantitative results, until the moving particles are trapped in the material or reach a threshold energy, which we have taken to be 1.0 eV [48–50].

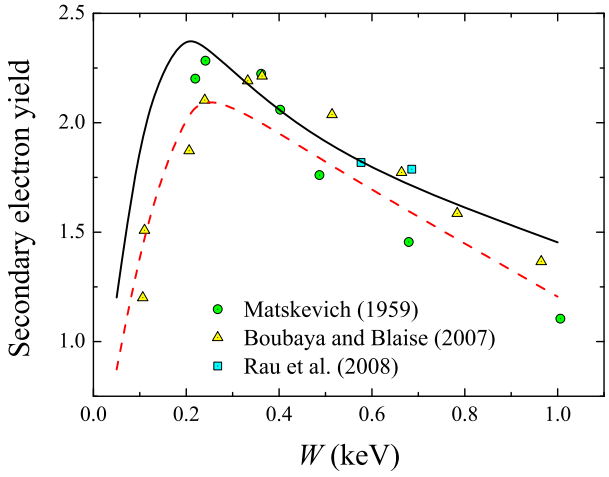


**Fig. 6.** Secondary electron yield of PMMA as a function of the primary electron kinetic energy obtained from the MELF-GOS model (solid line) and from the extended-Drude-GOS model (dashed line). Symbols correspond to experimental data [51–53].

## 4 Results and discussion

In this section we present the results for the propagation of the electrons produced in PMMA by low energy protons (50 keV–5 MeV). We concentrate in this low energy range, despite that initial energies used in hadron therapy are of the order of hundreds of MeV, since these are the typical energies of the protons when reaching the Bragg peak position, where the major part of the damage is expected.

The energy distribution of the secondary electrons generated by proton impact, at a given energy, is calculated by two optical data models to describe the target electronic excitation spectrum (MELF-GOS and extended-Drude-GOS). This magnitude will be the input quantity in the Monte Carlo simulation code to follow the motion of the electrons through the target. Also, the description of the electron slowing down in the simulation is done by two different ELF ($k \neq 0$) extension algorithms. Proceeding in this manner we have discussed the effects of the optical data model in the calculated radial energy deposition distributions.

In order to benchmark the Monte Carlo code to simulate the generation and the transport of energetic electrons in PMMA and the appropriate value of the parameters used, we calculate the secondary electron (SE) yield as a function of the electron energy and compare our results with experimental data. In Figure 6 we present the simulated SE yield obtained for the two descriptions of the target electronic excitation spectrum, namely the Mermin ELF (solid line) or the extended-Drude ELF (dashed line). The comparison with available experimental data [51–53], shown by symbols, is also presented. As it can be observed, due to the dispersion in the experimental data, the results obtained for the simulated SE yield for both ELF descriptions are compatible with experiments.

In Figure 7 we present the simulation of the radial energy deposition due to the energy delivered by all the

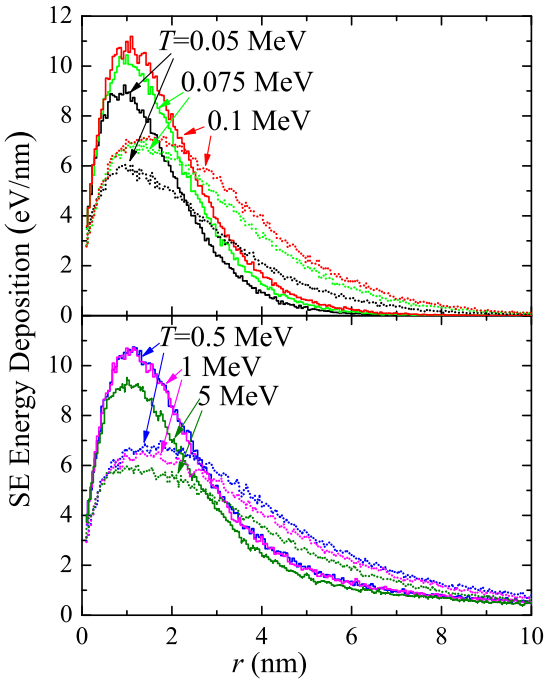


**Fig. 7.** Simulation of the secondary electron radial energy deposition due to 50 keV–5 MeV protons impinging on PMMA, as a function of the radial distance $r$ from the ion impact. These results have been obtained from the MELF-GOS model (solid lines) and from the extended-Drude model (dotted lines) used to describe the PMMA electronic response.

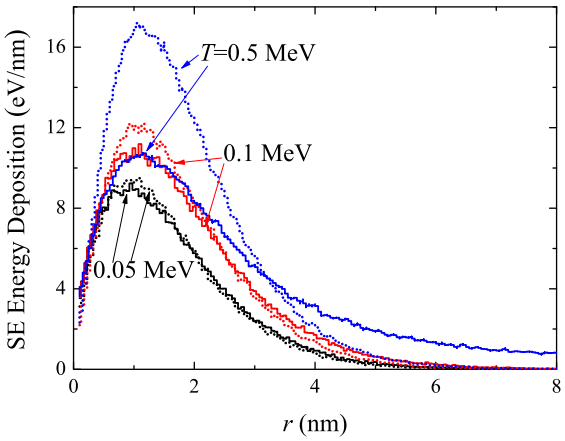


**Fig. 8.** Monte Carlo simulation of the radial energy depositions of secondary electron produced by 0.05 MeV, 0.1 MeV and 0.5 MeV protons impinging on PMMA, as a function of the radial distance $r$ from the ion impact, obtained from the MELF-GOS model. The simulations have been done with the actual initial energy distribution of the emitted electrons (solid lines) and with a single initial energy corresponding to the average energy of the emitted electrons (dotted lines).

electrons (secondary plus avalanche) generated by the incidence on PMMA of protons with energies between 50 keV and 5 MeV, which are typical proton energies at the Bragg peak. This allows the analysis of differences coming from the use of the Mermin and the extended-Drude ELF description of the target in the generation of secondary electrons and their transport through the medium. Our simulation shows that important differences appear in the radial energy deposition, which is larger and closer to the projectile track when the Mermin ELF is applied instead of the extended-Drude ELF. In the case of the MELF-GOS model the distance corresponding to the maximum energy deposition is around 1 nm (independent of the proton energy), whereas for the extended-Drude ELF this distance is displaced up to 1.85 nm. This implies that the MELF-GOS model predict a larger density of the deposited energy than the extended-Drude ELF, which could give a greater damage in the medium. The maximum value of the energy deposited by SE in the target increases from $T = 50$ keV up to 100 keV, remains constant from $T = 100$ keV up to 1 MeV, and decreases at $T = 5$ MeV. This behavior means that protons with energies from 100 keV up to 1 MeV are more efficient in the target energy deposition by the secondary electrons. In fact, the radial energy deposition spectrum is rather similar for proton with energies from $T = 100$ keV up to 1 MeV. The maximum value of the SE energy deposition at any proton energy is around 11 eV/nm for the MELF-GOS model whereas for the extended-Drude model it is about 7 eV/nm. For the Mermin ELF, the radial energy deposition decreases below 5% with respect to the maximum value at distances larger than 5 nm. However, when the extended-Drude model is used, the distances where the electron energies are deposited are practically twice the distances obtained for the MELF model. In all the cases the total energy deposition (that is the integral of the radial energy distribution) is the same for both ELF models.

Finally, to determine if the actual energy distribution of electrons generated by the proton impact plays some role in the simulation results, we present in Figure 8 the radial energy deposition in PMMA obtained when using the initial energy distribution of the secondary electrons generated by the proton impact (see Fig. 2) or the average energy of that distribution (see Fig. 4); now only the MELF-GOS method has been used to describe the electronic properties of PMMA. As it can be seen, for the lowest proton energy analyzed (50 keV), the differences between the simulations when using either the energy distributions or the average energy of the secondary electrons are insignificant. Nonetheless, these differences start to be more visible at 100 keV, and they are very sizeable at 500 keV. This behavior can be understood from the analysis of the SDCS; for higher proton energies, more energetic electrons can be generated, i.e., the energy distributions are wider, so the differences in the SE energy deposition between the average energy and the real energies of the electrons are larger.

## 5 Conclusions

In this work we have analyzed the production and propagation of secondary electrons generated by low energy

proton (50 keV–5 MeV) impact in the organic polymer PMMA, which is commonly used as a water or tissue phantom in ion beam cancer therapy dosimetry measurements, as well as a resist in nanolithographic techniques. To perform such analysis, we have produced secondary electron energy distributions for different proton energies, according to two different optical data models (MELF-GOS and extended-Drude-GOS methods), as explained in Section 2. Then, these energy distributions have been used as input for the event-by-event Monte Carlo simulation code described in Section 3, which, apart from including the electronic inelastic interactions (evaluated in the framework of the optical data models), also considers the other relevant interaction processes, namely, elastic scattering with target nuclei, electron-phonon interaction, and electron-polaron interaction.

This simulation code has been, first of all, benchmarked against SE yields, showing results in accordance with the available experimental information. Then, it has been used to calculate the radial energy deposition distributions around the tracks of protons. It has been shown that the choice of the optical data model (MELF-GOS or extended-Drude GOS) strongly influences the shape of the radial distributions, being much narrower when the MELF-GOS method, which is a much more accurate approach, is used. Furthermore, the effect of the actual energy distributions of electrons, as compared with their average energy, has been also analyzed. We found that, for proton energies below 50 keV, the energy distribution of electrons does not affect the final radial energy deposition distributions. Nonetheless, when the proton energies increase then the differences start to be noticeable. We also found that the SE energy deposition spectrum is maximum and constant for proton energies from $T = 100$ keV up to 1 MeV, which indicates that protons with those energies are more efficient in the energy deposition by secondary electrons.

Therefore, we conclude that the use of a proper optical data model, as the MELF-GOS method, is relevant for the evaluation of radial energy deposition distributions around proton tracks through the use of Monte Carlo simulations. The energy distributions provided by the ionization SDCS, as well as the inelastic inverse mean free path for electron propagation in PMMA, yield simulation results which notably differ from the ones obtained using simpler optical data models and average electron energies, thus stressing the importance of the use of detailed simulations, fed with proper electronic inelastic data, for the study of the effects of ion beams in organic materials at the nanometric scale.

This work has been supported by the Spanish Ministerio de Economía y Competitividad (Project FIS2014-58849-P) and by the Istituto Nazionale di Fisica Nucleare (INFN) through the Supercalcolo agreement with FBK. PdV acknowledges financial support from the European Union's FP7-People Program (Marie Curie Actions) within the Initial Training Network No. 608163 "ARGENT".

## References

1. G. Kraft, Prog. Part. Nucl. Phys. **45**, S473 (2000)
2. J.S. Loeffler, M. Durante, Nature Rev. Clin. Oncol. **10**, 411 (2013)
3. H. Paganetti, Phys. Med. Biol. **57**, R99 (2012)
4. D. Schardt, T. Elsässer, D. Schulz-Ertner, Rev. Mod. Phys. **82**, 383 (2010)
5. H. Nikjoo, S. Uehara, D. Emfietzoglou, A. Brahme, New J. Phys. **10**, 075006 (2008)
6. B. Boudaïffa, P. Cloutier, D. Hunting, M.A. Huels, L. Sanche, Science **287**, 1658 (2000)
7. M.A. Huels, B. Boudaïffa, P. Cloutier, D. Hunting, L. Sanche, J. Am. Chem. Soc. **125**, 4467 (2003)
8. H. Nikjoo, L. Linkbord, Phys. Med. Biol. **55**, R65 (2010)
9. R. Garcia-Molina, I. Abril, S. Heredia-Avalos, I. Kyriakou, D. Emfietzoglou, Phys. Med. Biol. **56**, 6475 (2011)
10. I. Abril, R. Garcia-Molina, P. de Vera, I. Kyriakou, D. Emfietzoglou, Adv. Quantum Chem. **65**, 129 (2013)
11. P. de Vera, I. Abril, R. Garcia-Molina, Appl. Radiat. Isotopes **83**, 122 (2014)
12. H. Palmans, J.E. Symons, J.-M. Denis, E.A. de Kock, D.T.L. Jones, S. Vynckier, Phys. Med. Biol. **47**, 3055 (2002)
13. M. Dapor, M. Ciappa, W. Fichtner, J. Micro Nanolithogr. MEMS MOEMS **9**, 023001 (2010)
14. P. de Vera, R. Garcia-Molina, I. Abril I, A.V. Solov'yov, Phys. Rev. Lett. **110**, 148104 (2013)
15. J. Lindhard, K. Dan. Vidensk. Selsk. Mat. Fys. Medd. **28**, 8 (1954)
16. D. Emfietzoglou, in *Interaction of Radiation with Matter*, edited by H. Nikjoo, S. Uehara, D. Emfietzoglou (CRC Press, Boca Raton, 2012)
17. P. de Vera, I. Abril, R. Garcia-Molina, A.V. Solov'yov, J. Phys.: Conf. Ser. **438**, 012015 (2013)
18. J.C. Moreno-Marín, I. Abril, S. Heredia-Avalos, R. Garcia-Molina, Nucl. Instrum. Methods Phys. Res. B **249**, 29 (2006)
19. J.J. Ritsko, L.J. Brillson, R.W. Bigelow, T.J. Fabish, J. Chem. Phys. **69**, 3931 (1978)
20. R. Garcia-Molina, I. Abril, I. Kyriakou, D. Emfietzoglou, in *Radiation Damage in Biomolecular Systems*, Biological and Medical Physics, Biomedical Engineering, edited by G.G. Gómez-Tejedor, M.C. Fuss (Springer, Dordrecht, 2012), Chap. 15
21. P. de Vera, I. Abril, R. Garcia-Molina, J. Appl. Phys. **109**, 094901 (2011)
22. J.C. Moreno-Marín, I. Abril, R. Garcia-Molina, Nucl. Instrum. Methods Phys. Res. B **193**, 30 (2002)
23. I. Abril, R. Garcia-Molina, C.D. Denton, I. Kyriakou, D. Emfietzoglou, Rad. Res. **175**, 247 (2011)
24. R.H. Ritchie, A. Howie, Philos. Magazine **36**, 463 (1977)
25. I. Abril, R. Garcia-Molina, C.D. Denton, J.F. Pérez-Pérez, N.R. Arista, Phys. Rev. A **58**, 357 (1998)
26. S. Heredia-Avalos, R. Garcia-Molina, J.M. Fernández-Varea, I. Abril, Phys. Rev. A **72**, 052902 (2005)
27. N.D. Mermin, Phys. Rev. B **1**, 2362 (1970)
28. U. Büchner, Phys. Stat. Sol. B **81**, 227 (1977)
29. D.J. Planes, R. Garcia-Molina, I. Abril, N.R. Arista, J. Elect. Spectrosc. Relat. Phenomena **82**, 23 (1996)
30. P.E. Batson, J. Silcox, Phys. Rev. B **27**, 5224 (1983)
31. C.D. Denton, I. Abril, R. Garcia-Molina, J.C. Moreno-Marín, S. Heredia-Avalos, Surf. Interface Anal. **40**, 1481 (2008)

32. H. Hayashi, N. Watanabe, Y. Udagawa, C.-C. Kao, J. Chem. Phys. **108**, 823 (1998)
33. N. Watanabe, H. Hayashi, Y. Udagawa, J. Phys. Chem. Solids **61**, 407 (2000)
34. W.E. Wilson, J.H. Miller, L.H. Toburen, S.T. Manson, J. Chem. Phys. **80**, 5631 (1984)
35. M.E. Rudd, T.V. Goffe, R.D. DuBois, L.H. Toburen, Phys. Rev. A **31**, 492 (1985)
36. M.A. Bolorizadeh, M.E. Rudd, Phys. Rev. A **33**, 888 (1986)
37. H. Nikjoo, S. Uehara, D. Emfietzoglou, F.A. Cucinotta, Rad. Meas. **41**, 1052 (2006)
38. E. Surdutovich, A.V. Solov'yov, Eur. Phys. J. D **68**, 353 (2014)
39. N.F. Mott, Proc. R. Soc. London Ser. **124**, 425 (1929)
40. J.M. Fernández-Varea, R. Mayol, D. Liljequist, F. Salvat, J. Phys.: Condens. Matter **5**, 3593 (1993)
41. S. Tanuma, C.J. Powell, D.R. Penn, Surf. Interface Anal. **21**, 165 (1993)
42. R.F. Roberts, D.L. Allara, C.A. Pryde, D.N.E. Buchanan, N.D. Hobbins, Surf. Interface Anal. **2**, 5 (1980)
43. H. Fröhlich, Adv. Phys. **3**, 325 (1954)
44. J.P. Ganachaud, A. Mokrani, Surface Sci. **334**, 329 (1995)
45. J. Llacer, E.L. Garwin, J. Appl. Phys. **40**, 2766 (1969)
46. M. Dapor, Nucl. Instrum. Methods Phys. Res. B **269**, 1668 (2011)
47. M. Dapor, *Transport of Energetic Electrons in Solids: Computer Simulation with Applications to Materials Analysis and Characterization*, Springer Tracts in Modern Physics (Springer, Berlin, 2014), Vol. 257
48. R. Shimizu, Z.-J. Ding, Rep. Prog. Phys. **55**, 487 (1992)
49. J.Ch. Kuhr, H.J. Fitting, J. Electron Spectrosc. Relat. Phenom. **105**, 257 (1999)
50. M. Dapor, B.J. Inkson, C. Rodenburg, J.M. Rodenburg, Europhys. Lett. **82**, 30006 (2008), Erratum: M. Dapor, B.J. Inkson, C. Rodenburg, J.M. Rodenburg, Europhys. Lett. **82**, 49901 (2008)
51. T.L. Matskevich, Fiz. Tverd. Tela Adad. Nauk. **1**, 277 (1959)
52. M. Boubaya, G. Blaise, Eur. Phys. J. Appl. Phys. **37**, 79 (2007)
53. E.I. Rau, E.N. Evstafeva, M.V. Adrianov, Phys. Solid State **50**, 599 (2008)